LkHα 198 an opening angle of 45° without limb brightening. Thus, our observations do not support the presence of evacuated cavities in the envelope of LkHα 198. The observed morphology can instead be explained by the illumination of a cavity-free, rotationally flattened envelope by the central star; the bipolar appearance would then arise from light escaping along the path of least optical depth. However, these cavity-free infalling envelope models have opening angles that increase with wavelength, whereas we observe a constant opening angle, suggesting a geometric rather than optical depth origin for the observed morphology. This discrepancy may be resolvable by varying the dust particle properties.

On the basis of these observations, LkHα 233 is the more evolved of the two systems, with well-defined cavities swept out by bipolar outflow and bisected by a very dark lane. LkHα 198 is a less evolved system, which is only in the early stages of developing bipolar cavities and possesses lower extinction in the apparent disk midplane.

The observed circumstellar environments are consistent with the rotationally flattened infall envelopes models developed for T Tauri stars, indicating that the process of envelope collapse has similar phases, despite the large disparities in mass and luminosity between these two classes of young stars. This morphological similarity leads us to infer that the conservation and transport of angular momentum is the dominant physical process for both classes of stars. Alternate formation pathways have been suggested for OB stars that invoke new physical mechanisms, such as magnetohydrodynamic turbulence (*31*) or stellar mergers (*32*). The Herbig Ae stars studied here appear to be below the mass threshhold at which such effects become important.

References and Notes

1. W. Happer, G. J. MacDonald, C. E. Max, F. J. Dyson, *J. Opt. Soc. Am.* **11**, 263 (1994).
2. L. A. Hillenbrand, S. E. Strom, F. J. Vrba, J. Keene, *Astrophys. J.* **397**, 613 (1992).
3. P. Bastien, *Astrophys. J.* **317**, 231 (1987).
4. D. A. Weintraub, A. A. Goodman, R. L. Akeson, in *Protostars and Planets IV*, V. Mannings, A. P. Boss, S. S. Russell, Eds. (Univ. of Arizona Press, Tucson, AZ, 2000), pp. 247–271.
5. C. Max *et al.*, *Science* **277**, 1649 (1997).
6. J. P. Lloyd *et al.*, *Proc. SPIE* **4008**, 814 (2000).
7. Additional information on materials and methods is available as supporting material on *Science* Online.
8. D. E. Potter *et al.*, *Astrophys. J.* **540**, 422 (2000).
9. J. R. Kuhn, D. Potter, B. Parise, *Astrophys. J.* **553**, L189 (2001).
10. W. Li, N. J. Evans, P. M. Harvey, C. Colome, *Astrophys. J.* **433**, 199 (1994).
11. J. Canto, L. F. Rodriguez, N. Calvet, R. M. Levreault, *Astrophys. J.* **282**, 631 (1984).
12. D. Corcoran, T. P. Ray, P. Bastien, *Astron. Astrophys.* **293**, 550 (1995).
13. R. Hajjar, P. Bastien, *Astrophys. J.* **531**, 494 (2000).
14. G. Sandell, D. A. Weintraub, *Astron. Astrophys.* **292**, L1 (1994).
15. C. D. Koresko, P. M. Harvey, J. C. Christou, R. Q. Fugate, W. Li, *Astrophys. J.* **485**, 213 (1997).
16. P. O. Lagage *et al.*, *Astrophys. J. Lett.* **417**, L79+ (1993).
17. M. Fukagawa *et al.*, *J. Psychiatry Neurosci.* **54**, 969 (2002).
18. T. Henning, A. Burkert, R. Launhardt, C. Leinert, B. Stecklum, *Astron. Astrophys.* **336**, 565 (1998).
19. S. Terebey, F. H. Shu, P. Cassen, *Astrophys. J.* **286**, 529 (1984).
20. C. Aspin, M. J. McCaughrean, I. S. McLean, *Astron. Astrophys.* **144**, 220 (1985).
21. M. Corcoran, T. P. Ray, *Astron. Astrophys.* **336**, 535 (1998).
22. F. Shu *et al.*, *Astrophys. J.* **429**, 781 (1994).
23. F. H. Shu, F. C. Adams, S. Lizano, *Annu. Rev. Astron. Astrophys.* **25**, 23 (1987).
24. F. Palla, S. W. Stahler, *Astron. J.* **418**, 414 (1993).
25. V. Mannings, A. I. Sargent, *Astrophys. J.* **490**, 792 (1997).
26. V. Mannings, D. W. Koerner, A. I. Sargent, *Nature* **388**, 555 (1997).
27. J. di Francesco, N. J. Evans, P. M. Harvey, L. G. Mundy, H. M. Butner, *Astrophys. J.* **432**, 710 (1994).
28. A. Natta *et al.*, *Astron. Astrophys.* **371**, 186 (2001).
29. B. A. Whitney, K. Wood, J. E. Bjorkman, M. J. Wolff, *Astrophys. J.* **591**, 1049 (2003).
30. B. A. Whitney, K. Wood, J. E. Bjorkman, M. Cohen, *Astrophys. J.* **598**, 1079 (2003).
31. C. F. McKee, J. C. Tan, *Astrophys. J.* **585**, 850 (2003).
32. I. A. Bonnell, M. R. Bate, H. Zinnecker, *Mon. Not. R. Astron. Soc.* **298**, 93 (1998).
33. We thank the Lick Observatory staff who assisted in these observations, including T. Misch, K. Chloros, and J. Morey; the many individuals who have contributed to making the laser guide star system a reality; and B. Whitney for providing us with electronic versions of models. Onyx Optics fabricated our YLF Wollaston prisms. Supported in part by NSF Science and Technology Center for Adaptive Optics, managed by the University of California at Santa Cruz under cooperative agreement AST-9876783 and also under the auspices of the U.S. Department of Energy, National Nuclear Security Administration, by the University of California, Lawrence Livermore National Laboratory, under contract W-7405-Eng-48. P.K. received additional support from the NASA Origins Program (grant NAG5-11769). M.D.P. is supported by a NASA Michelson Graduate Fellowship, under contract to the Jet Propulsion Laboratory (JPL). JPL is managed for NASA by the California Institute of Technology.

Single-Crystal Nanorings Formed by Epitaxial Self-Coiling of Polar Nanobelts

Xiang Yang Kong, Yong Ding, Rusen Yang, Zhong Lin Wang*

Freestanding single-crystal complete nanorings of zinc oxide were formed via a spontaneous self-coiling process during the growth of polar nanobelts. The nanoring appeared to be initiated by circular folding of a nanobelt, caused by long-range electrostatic interaction. Coaxial and uniradial loop-by-loop winding of the nanobelt formed a complete ring. Short-range chemical bonding among the loops resulted in a single-crystal structure. The self-coiling is likely to be driven by minimizing the energy contributed by polar charges, surface area, and elastic deformation. Zinc oxide nanorings formed by self-coiling of nanobelts may be useful for investigating polar surface–induced growth processes, fundamental physics phenomena, and nanoscale devices.

Self-assembly of nanocrystals can be driven by van der Waals forces and hydrogen bonding among the passivating organic molecules on the particle surfaces (*1–3*). For inorganic nanostructures that expose charge-polarized surfaces, such as nanobelts of oxides like ZnO (*4*), electrostatic forces can drive self-assembly, especially in gas-phase environments where these forces are unscreened by solvents. For crystalline nanomaterials grown in a solid-vapor environment, one type of polar charge–induced helical and spiral ZnO structure was previously reported (*5*). We now report a distinct nanoring structure that is formed by spontaneous self-coiling of a polar nanobelt during growth. Nanoring growth

appears to be initiated by circular folding of a nanobelt driven by long-range electrostatic interactions. Short-range chemical bonding among the loops leads to the final single-crystalline structure. The self-coiling is driven by minimizing the energy contributed by polar charges, surface area, and elastic deformation.

Single-crystal nanorings of ZnO were grown by a solid-vapor process. The raw material was a mixture of ZnO (melting point 1975°C), indium oxide, and lithium carbonate powders at a weight ratio of 20:1:1, and it was placed at the highest temperature zone of a horizontal tube furnace. Before heating to a desired temperature of 1400°C, the tube furnace was evacuated to ~10^{-3} torr to remove the residual oxygen. The source materials were then heated to 1400°C at a heating rate of 20°C/min. ZnO decomposes into Zn^{2+} and O^{2-} at high temperature (1400°C) and low pressure (~10^{-3} torr), and this decomposition process is the key step for controlling the anisotropic growth of the nanobelts. After a few

School of Materials Science and Engineering, Georgia Institute of Technology, Atlanta, GA 30332–0245 USA.

*To whom correspondence should be addressed. E-mail: zhong.wang@mse.gatech.edu

minutes of evaporation and decomposition, the Ar carrier gas was introduced at a flux of 50 standard cubic centimeters per minute. The synthesis process was conducted at 1400°C for 30 min. The condensation products were deposited onto a silicon substrate placed in a temperature zone of 200° to 400°C under Ar pressure of 500 torr. The as-synthesized samples were analyzed by scanning electron microscopy (SEM) and high-resolution transmission electron microscopy (HRTEM).

The as-synthesized sample was composed of many freestanding nanorings at a significant percentage (~20 to 40%) of the yield (Fig. 1A) and 70% reproducibility from run to run. The rings had typical diameters of ~1 to 4 μm and thin, wide shells that were ~10 to 30 nm thick. SEM images recorded at high magnification clearly show the perfect circular shape of the complete rings, with uniform shapes and flat surfaces (Fig. 1B). Energy-dispersive x-ray spectroscopy analysis indicated that the nanorings were ZnO (6).

Two types of nanoring structures were found. The type I structure is presented in Fig. 2. A TEM image (Fig. 2A) indicates that the nanoring is a single-crystal entity with nearly perfect circular shape, although there is electron diffraction (ED) contrast caused by non-uniform deformation along the circumference. The single-crystal structure referred to here means a complete nanoring that is made of a single-crystal ribbon bent evenly at the curvature of the nanoring. Tilting the nanoring by ~20° clearly shows the single-crystal circular shape (Fig. 2B). The corresponding dark-field TEM image (Fig. 2C) shows the contrast produced by the equally bending lines across the width of the nanoring (Fig. 2C), which is caused by the tilting of the atomic plane with respect to the electron beam. Deformation in the nanometer-thick ribbon does not necessarily introduce dislocations. An ED pattern recorded from the center of the nanoring (area a_1 in Fig. 2A) shows that the radial direction of the nanoring is $[1\bar{2}10]$, the tangential direction is $[10\bar{1}0]$, and the nanoring axis is [0001]. HRTEM images recorded from the three corners of the image in Fig. 2A (areas d, e, and f in Fig. 2, D to F, respectively) show the distribution of the equally spaced planar defects nearly parallel to the nanoring plane. The planar defects align from the top of the nanoring to the bottom without interruption (Fig. 2, D and F). The trace of the coiling nanobelt is best seen through the side of the nanoring, as indicated by arrowheads in Fig. 2F. The entire nanoring is a single crystal, although the quality of the crystallinity varies slightly across the width of the nanoring, as shown in the enlarged TEM image in Fig. 2G.

The nanoring is made of coaxial, uniradial, epitaxial coiling of a nanobelt. Careful examination of the image in Fig. 2A shows a loose end of the raveling nanobelt, as indicated by a red arrowhead (7). The coiling of this nanobelt to form

the nanoring is shown in the enlarged image in Fig. 2F, as marked by an arrowhead at the top. Examination of the other side of the nanoring found the other loose end of the nanobelt (indicated by an arrowhead in Fig. 2E). The ED

pattern recorded from the loose end of the nanobelt, as circled in the enlarged area a_3, indicates that the nanobelt has a growth direction of $[10\bar{1}0]$, side surfaces $\pm(1\bar{2}10)$, and top/bottom surfaces $\pm(0001)$. The nanoring is made of coil-
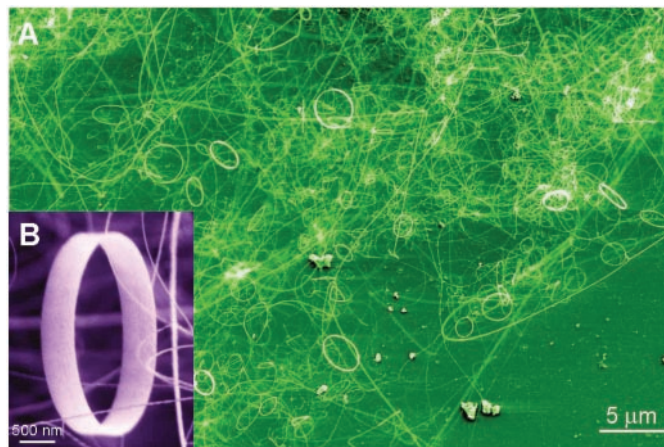

Fig. 1. (A) Low-magnification SEM image of the as-synthesized ZnO nanorings. (B) High-magnification SEM image of a freestanding single-crystal ZnO nanoring, showing uniform and perfect geometrical shape. The ring diameter is 1 to 4 μm, the thickness of the ring is 10 to 30 nm, and the width of the ring shell is 0.2 to 1 μm.

Fig. 2. Structure of the type I ZnO single-crystal nanoring. (A) A TEM image of a ZnO nanoring viewed with the electron beam parallel to the plane of the nanoring. (a_1) An ED pattern recorded from area a_1 marked in (A). (a_2) Enlargement of area a_2 marked in (A), showing a loose end at the left-hand side. (a_3) An ED pattern recorded from the loose end (area a_3 marked in a_2). (B and C) Bright-field and dark-field TEM images recorded from the nanoring after it was tilted by ~15°. (b) The ED pattern recorded from area b marked in (B). (D to F) are the larger images from areas d to f, respectively, marked in (A), after the nanoring was slightly tilted. (G) An enlarged TEM image of the nanoring tilted by ~10°. (H) An enlargement of area h indicated in (C), illustrating a uniform distribution of planar defects across the entire width of the nanoring. (I) HRTEM image recorded from the nanoring when the incident electron beam was parallel to the ring plane, showing planar defects inside the nanobelt and at the interface between the coiled loops. The width of the nanobelt is indicated.
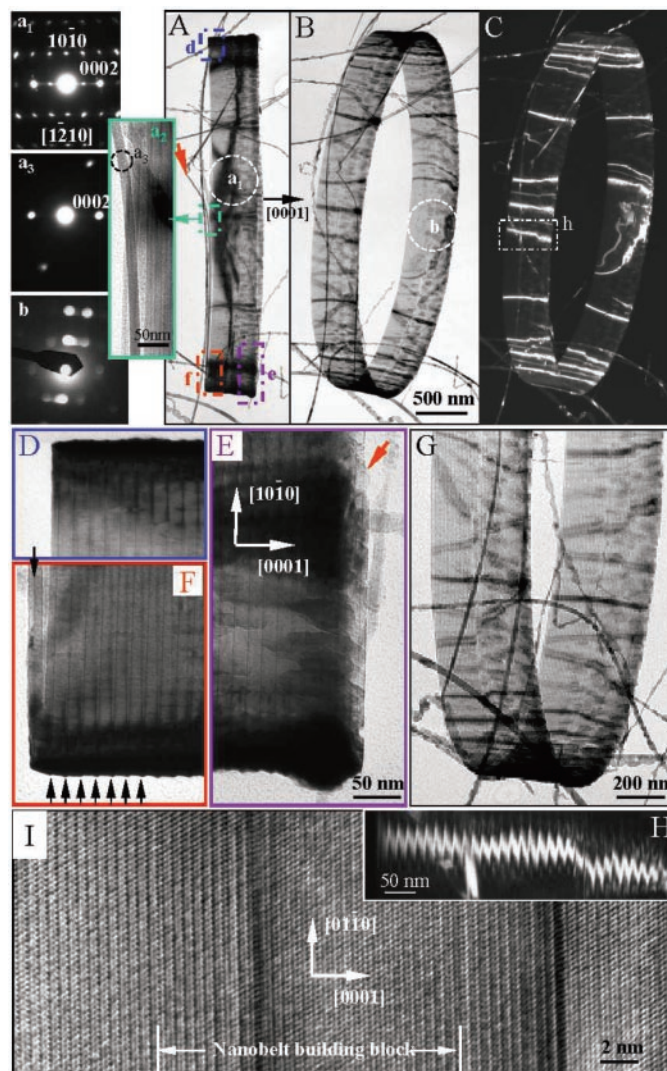
ing loops of the nanobelt, as in a child's "Slinky" spring (7), by interfacing its (0001)-Zn and (000$\bar{1}$)-O planes at the same crystallographic orientation. The coiling of the nanobelt introduces a small helical angle of ~0.3°; this small rotation is hardly detectable by the ED pattern.

Fig. 3. Structure of the type II ZnO single-crystal nanoring. (**A** and **B**) Bright-field and dark-field TEM images recorded from the nanoring, with the incident electron beam parallel to the ring plane. (**C**) ED pattern recorded from the nanoring. The pattern shows vertical mirror symmetry, and the extra diffraction spots at the two sides are from the cylindrical bending of the single-crystal ribbon. (**D**) HRTEM image recorded from the central symmetric line in (A). (**E**) Enlarged TEM images from area e marked in (A), showing the coiling layers. The total number of loops forming this nanoring is 100. (**F**) Dark-field TEM image recorded from the nanoring after it was tilted by 15°.
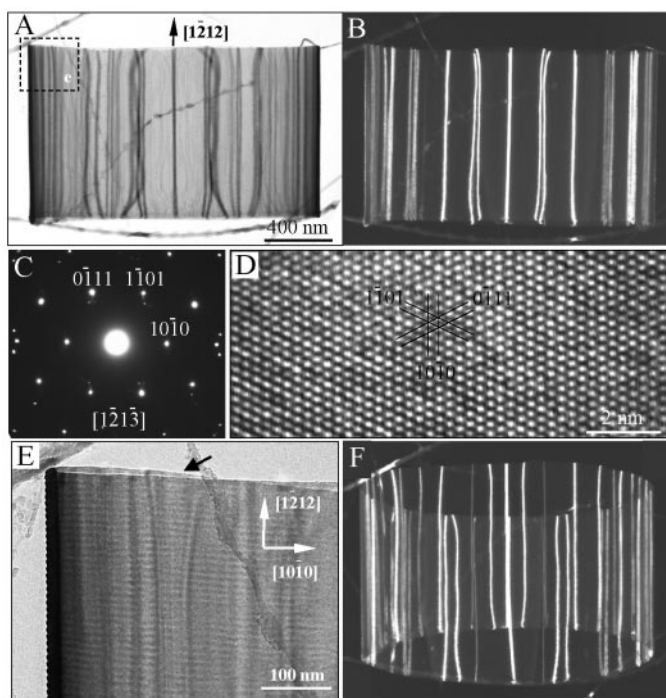

Fig. 4. (**A**) Structure model of ZnO and the corresponding crystal planes discussed in the text, showing the ±(0001) polar surfaces. (**B** to **D**) Proposed growth process and corresponding experimental results showing the initiation and formation of the single-crystal nanoring via self-coiling of a polar nanobelt. The nanoring is initiated by folding a nanobelt into a loop with overlapped ends driven by long-range electrostatic interactions among the polar charges. Short-range chemical bonding stabilizes the coiled ring structure, and the spontaneous self-coiling of the nanobelt is driven by minimizing the energy contributed by polar charges, surface area, and elastic deformation. (**E**) Calculated energy gain ($\Delta E = \Delta E_{\text{Deform}} + \Delta E_{\text{Electro}}$) before and after folding of a straight polar nanobelt into a loop-structured nanoring as a function of the ring radius and the number of loops. Nanobelt width = 20 nm, thickness = 16 nm, Young's modulus = 50 GPa, and surface charge density $|\sigma| = 0.057$ C/m². The calculation gives the threshold radius under which initiation of the nanoring structure is energetically unfavorable. The smallest nanoring observed has $D = 0.8$ μm.
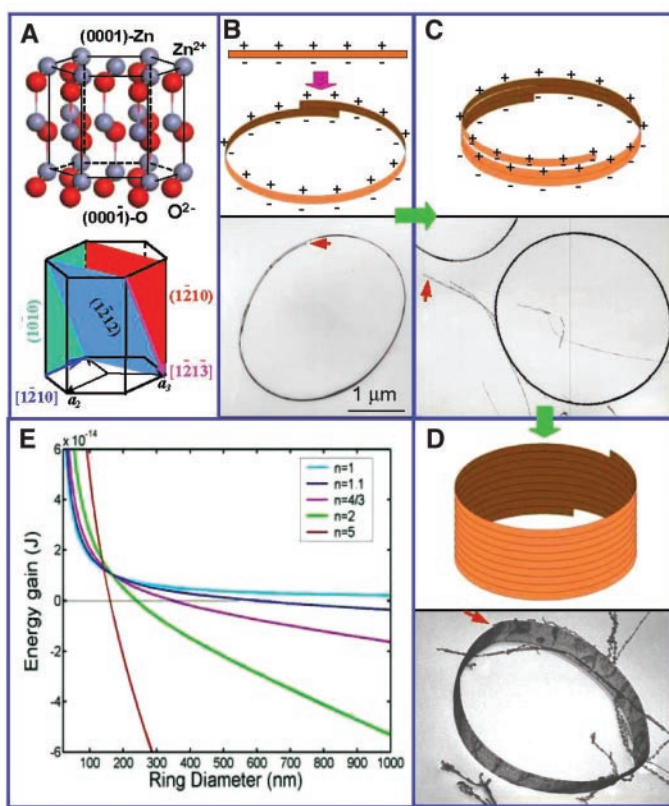
The loose end of the nanobelt in Fig. 2F has a (0001) planar defect located close to the middle of its width, which suggests that the planar defect was produced during the nanobelt's growth and is the key for producing the fastest growth of the nanobelt along its axial direction (8, 9). We counted 33 coiling loops in the dark-field TEM image displayed in Fig. 2H. HRTEM indicates that, besides the planar defect inside the nanobelt, a stacking fault is formed at the interface between the adjacent loops, which is introduced to match the lattices of the Zn-terminated and O-terminated (0001) polar surfaces (10). The interface between the loops is coherent, epitaxial, and chemically bonded (Fig. 2I).

The type II nanoring structure is presented in Fig. 3. Bright-field (Fig. 3A) and dark-field (Fig. 3B) TEM images show that the complete nanoring is a single crystal, which again implies that the nanoring shell is a uniformly deformed, single-crystal ribbon around the circumference. Electron diffraction (Fig. 3C) and the corresponding HRTEM image recorded from the central region (Fig. 3D) show that the radial direction of the nanoring is [1$\bar{2}$1$\bar{3}$], the tangential direction is [10$\bar{1}$0], and the nanoring plane is (1$\bar{2}$12) (see the model in Fig. 4A), and there is no dislocation in the volume. Figure 3E displays the enlarged view of the corner indicated in Fig. 3A, which shows an end of the nanobelt (indicated by an arrowhead) and the screw coiling of the nanobelt. The pitch distance for the coiling is 10 nm, and the total number of loops is 100. The contrast produced by stacking faults parallel to the nanoring plane is visible, but the (0001) stacking fault plane is at an angle of ~28° from the nanoring axis. The nanoring has a thin crystal wall ~15 nm thick, as clearly shown by tilting the nanoring by 15° (Fig. 3F).

The growth of the nanoring structures can be understood on the basis of the polar surfaces of the ZnO nanobelt. The wurtzite-structured ZnO crystal is described schematically as a number of alternating planes composed of tetrahedral coordinated O^{2-} and Zn^{2+} ions, stacked alternatively along the c axis (Fig. 4A). The oppositely charged ions produce positively charged (0001)-Zn and negatively charged (000$\bar{1}$)-O polar surfaces. The polar nanobelt, which is the building block of the nanoring, grows along [10$\bar{1}$0], with side surfaces ±(1$\bar{2}$10) and top/bottom surfaces ±(0001) (4), and has a typical width of ~15 nm and thickness of ~10 nm (7). The planar defect parallel to (0001) lowers the nanobelt energy and is key to producing the fastest anisotropic growth along [10$\bar{1}$0], but it does not affect the intrinsic polarity of the nanobelt. Therefore, the nanobelt has polar charges on its top and bottom surfaces (Fig. 4B). If the surface charges are uncompensated for during growth (11), the nanobelt may tend to fold itself as it lengthens, in order to minimize the area of the polar surface. One possible way to reduce the electrostatic energy is

to interface the positively charged (0001)-Zn plane (top surface) with the negatively charged (000$\bar{1}$)-O plane (bottom surface), resulting in neutralization of the local polar charges and in reduced surface area, thus forming a loop with an overlapped end (Fig. 4B). The radius of the loop may be a result of how the nanobelt folds during its initial growth, but the size of the loop cannot be too small to reduce the elastic deformation energy.

The total energy involved in the process comes from polar charges, surface area, and elastic deformation (12). The long-range electrostatic interaction is likely to be the initial driving force for folding the nanobelt to form the first loop on which subsequent growth is based. Calculations have been made to assess the possibility of balancing the increased elastic deformation energy (ΔE_{Deform}) by the decreased electrostatic energy ($\Delta E_{\text{Electro}}$) at the initiation of the nanoring structure (7) (Fig. 4E). If a nanobelt is folded to form a single-loop complete ring ($n = 1$), the energy gain ΔE ($\Delta E = \Delta E_{\text{Deform}} + \Delta E_{\text{Electro}}$) is positive regardless of the size of the loop, suggesting that a single-loop complete ring is energetically unfavorable. For a 10% overlapped nanoring ($n = 1.1$), the nanoring structure is energetically possible if its diameter (D) is larger than 600 nm. It is thus possible to form a single-looped nanoring with overlapped ends at the beginning of the growth caused by fluctuation (Fig. 4B). For a 33% overlapped nanoring ($n = 4/3$), the nanoring structure is possible if D is larger than 360 nm. The diameters of the experimentally observed nanorings are in the range of 0.8 to 4 μm, and no ring has $D < 0.8$ μm. From the SEM images, we believe that the first step (Fig. 4B) occurs before the nanoring lands on the substrate.

The presence of a planar defect within the nanobelt (Fig. 2F) is likely to be the key to producing the fast growth of the nanobelt along [10$\bar{1}$0], because it lowers the energy in the wurtzite-structured lattice (8). Planar defects may be initiated by impurity atoms, such as Li and In, introduced into the raw material. As growth continues, the nanobelt may be naturally attracted to the rim of the nanoring by electrostatic interactions and then extend itself parallel to the rim of the nanoring to neutralize the local polar charge and reduce the surface area, resulting in the formation of a self-coiled, coaxial, uniradial, multilooped nanoring structure. The self-assembly is spontaneous, which means that the self-coiling along the rim proceeds as the nanobelt grows. The reduced surface area and the formation of chemical bonds (a short-range force) between the loops stabilize the coiled structure. The width of the nanoring increases as more loops wind along the nanoring axis (Fig. 4C), and all of them remain in the same crystal orientation.

Because growth is carried out in the temperature region from 200° to 400°C, "epitaxial sintering" (13) of the adjacent loops forms a single-crystal cylindrical nanoring structure, and the loops of the nanobelt are joined by chemical bonds as a single entity. The loops that were coiled first remained at the growth temperature for a longer time, resulting in higher crystallinity, whereas the ones that wound on later had less time for sintering and thus had relatively poorer crystallinity, forming the structure in Fig. 2G, with two contrast regions across the width of the nanoring. Finally, as the growth time was extended, the entire nanoring exhibited high-quality crystallinity, as shown by the diffraction contrast in Fig. 4D. A uniradial and perfectly aligned coiling is energetically favorable because of the complete neutralization of the local polar charges inside the nanoring and the reduced surface area. The entire growth process may have no relation to the substrate used for collecting the sample. The thinness of the nanoring also prevents the determination of its polarity by convergent-beam ED (14).

The coiling process presented in Fig. 4 unifies the two types of nanoring structures described in Figs. 2 and 3. If the (0001) polar surface of the ZnO nanobelt is parallel to the ring plane, self-coiling of the nanobelt at a radial direction of [1$\bar{2}$10] forms the type I structure in Fig. 2. Alternatively, if the nanobelt is tilted toward the nanoring center so that the radial direction is [1$\bar{2}$1$\bar{3}$] (15), self-coiling of the nanobelt produces the type II structure in Fig. 3. The tilting of the nanobelt may reduce the elastic deformation energy.

The model presented here can also be adopted to explain the helical nanostructure reported previously (5). If the nanobelt in Fig. 4B is flipped by 90° so that the radial direction of the nanoring is [0001], which means that the polarization is in the radial direction, a bending of the nanobelt into a circle slightly reduces the electrostatic energy, possibly in favor of forming an in-plane spiral nanoring (5). Alternatively, as a result of preserved polar charges on the inner and outer arc surfaces, the circular loops of the nanobelt cannot be densely packed into a single-crystal coil structure because of the electrostatic repulsion among them; instead, a helical structure would be formed, with a pitch distance of 200 to 500 nm [much larger than the width (~20 nm) or thickness (~10 nm) of the nanobelt], which is suggested to be a result of balancing the electrostatic repulsive force between the loops and the elastic deformation force.

The polar charge–induced nanorings presented here have potential applications in investigating fundamental physical phenomena, such as the Aharonov-Bohm oscillations in exciton luminescence (16). The piezoelectric and semiconducting properties of ZnO predict that the nanorings could be used as nanoscale sensors, transducers, and resonators.

References and Notes

1. C. B. Murray, C. R. Kagan, M. G. Bawendi, *Science* **270**, 1335 (1995).
2. R. L. Whetten *et al.*, *Adv. Mater.* **8**, 428 (1996).
3. J. F. Banfield, S. A. Welch, H. Z. Zhang, T. T. Ebert, R. L. Penn, *Science* **289**, 751 (2000).
4. Z. W. Pan, Z. R. Dai, Z. L. Wang, *Science* **291**, 1947 (2001).
5. X. Y. Kong, Z. L. Wang, *Nano Lett.* **3**, 1625 (2003).
6. Energy-dispersive x-ray spectroscopy has a detection limit of typically 1 to 2 atomic %. It may not detect impurities with a concentration lower than 2%.
7. See supporting material on *Science* Online.
8. Planar defects usually reduce the energy for the nanostructure, and it is easy to form during the growth of one-dimensional oxide nanostructures. Once formed, it leads to the fastest growth along a direction parallel to the defect plane. For a ZnO nanobelt growing along [10$\bar{1}$0], a single stacking fault is always present (4).
9. Recent study has also shown that the presence of a stacking fault is the key for forming Ag disks (17).
10. Wurtzite structure has four different types of stacking faults (18). The stacking fault at the nanobelt interface is type I. Type I and type III stacking faults have the lowest energy.
11. The local deposition temperature is ~200° to 400°C, which is high enough to prevent physical adsorption of molecules on the surface during growth. Thus, the polar charges on the surface are likely uncompensated for and are electrostatically effective for aligning the oppositely charged surfaces of the nanobelt during growth.
12. There are three components of energy involved in the formation of ring structure: electrostatic interaction energy among the polar charges, surface area energy due to the decrease in surface area after chemically bonding the loops, and elastic deformation energy due to bending. The former two are usually called the surface energy, which includes the contribution from surface tension, but we separate them here for the convenience of discussion in the text. Electrostatic and deformation forces are long-range interactions, and chemical bonding is a short-range interaction. Self-coiling is possible if the decreased electrostatic energy surpasses the increased elastic deformation energy, which is the case for a thin and narrow nanobelt.
13. Sintering in ceramics usually involves mass transport and diffusion. By "epitaxial sintering" here, we mean that the two loops are chemically bonded epitaxially with the same crystal orientation, and there may be no diffusion involved. As the nanobelt grew along its axial direction as guided by the planar defect, it was being bonded down on the rim of the ring by electrostatic interaction. Because the melting point for a nanostructure can be as low as one-third of its bulk melting point, and the temperature required for sintering is usually one-third of the melting temperature, it is thus possible to chemically join the loops at 200° to 400°C.
14. In principle, the polarity of the surfaces can be determined by convergent beam ED (CBED) (19), but it requires a specimen thickness of 50 nm or more to enhance the dynamic scattering effect. The 20-nm thickness of the rim of the nanoring is insufficient for CBED analysis.
15. Among the possible glide systems for hexagonal close-packed structure, (0001), [1$\bar{2}$10]; and (1$\bar{2}$12), [1$\bar{2}$1$\bar{3}$] are the two possible systems, which correspond to the cases presented in Figs. 2 and 3, respectively [see (20)].
16. R. A. Römer, M. E. Taikh, *Phys. Stat. Sol. B* **221**, 535 (2000).
17. V. Germain, J. Li, D. Ingert, Z. L. Wang, M. P. Pileni, *J. Phys. Chem. B* **107**, 8717 (2003).
18. C. Stampfl, C. G. Van de Walle, *Phys. Rev. B* **57**, R15052 (1998).
19. F. Vigue, P. Vennegues, S. Vezian, M. Laugt, J.-P. Faurie, *Appl. Phys. Lett.* **79**, 194 (2001).
20. L. A. Shuvalov, Ed., *Modern Crystallography IV, Springer Series in Solid-State Sciences 37* (Springer-Verlag, New York, 1988), p. 109.
21. Support was provided by NSF (DMR-9733160), the NASA Vehicle Systems Program, and the Department of Defense Research and Engineering (DDR&E) program. We thank R. L. Snyder and J. Z. Zhang for comments.